



SPE-97792

Multiple application of image log data to EOR planning in the Cooper Basin, Australia.

Scott Mildren, SPE, JRS Petroleum Research, Jamie Burgess, Santos Ltd and Jeremy Meyer, SPE, JRS Petroleum Research

Copyright 2005, Society of Petroleum Engineers

This paper was prepared for presentation at the SPE International Improved Oil Recovery Conference in Asia Pacific held in Kuala Lumpur, Malaysia, 5–6 December 2005.

This paper was selected for presentation by an SPE Program Committee following review of information contained in an proposal submitted by the author(s). Contents of the paper, as presented, have not been reviewed by the Society of Petroleum Engineers and are subject to correction by the author(s). The material, as presented, does not necessarily reflect any position of the Society of Petroleum Engineers, its officers, or members. Papers presented at SPE meetings are subject to publication review by Editorial Committees of the Society of Petroleum Engineers. Electronic reproduction, distribution, or storage of any part of this paper for commercial purposes without the written consent of the Society of Petroleum Engineers is prohibited. Permission to reproduce in print is restricted to a proposal of not more than 300 words; illustrations may not be copied. The proposal must contain conspicuous acknowledgment of where and by whom the paper was presented. Write Librarian, SPE, P.O. Box 833836, Richardson, TX 75083-3836, U.S.A., fax 01-972-952-9435.

Abstract

Reservoir geometry, natural fracture networks and *in situ* stress directly impact on the planning and implementation of flooding operations. Image logs were acquired from two wells in Field A, the Cooper Basin, with three main objectives in mind: increase confidence on the distribution of oil reservoir sand prior to in-fill drilling; quantify natural fracture populations and assess their possible contribution to production from a tight reservoir, and; quantify the contemporary stress regime and consider its bearing on idealised flow direction.

Tectonic tilt and palaeocurrent indicators were identified in conjunction with natural fractures and *in situ* stress features from both wells. Palaeocurrent flow directions confirmed a dominant transport direction to the south. However, sediment transport within the Tirrawarra Sandstone reservoir is clearly to the northeast parallel to the strike of the Field A structure. This implies enhanced permeability parallel to this direction due to grain stacking.

Natural fracture density is more enhanced at the crest of the structure than the flanks and the dominant 065°N natural fracture trend is predicted to have greater hydraulic conductivity with respect to the *in situ* stress field.

The *in situ* stress field was determined to be strike-slip with σ_{Hmax} oriented approximately 117°N defining a third permeability enhancement associated with Field A. Without further knowledge of the relative magnitudes of each of these permeability enhancements, it is recognized that EOR patterns planned in an east-west orientation will maximize flooding and sweep efficiency within the Tirrawarra Sandstone oil reservoir.

Introduction

Field A is a NE-SW oriented body comprised of a low permeability (0.1 – 1.0 mD) tight sandstone reservoirs with 7-

11% porosity (**Fig. 1**). The Tirrawarra Sandstone reservoir has been produced by depletion drive and initial pressures of approximately 4200 psig has been drawn-down to 3150 psig in the NE and 2700-2800 psig in the SW. With production since 1983, EOR procedures are being considered to improve the current 3-4% recovery of the original oil-in-place.

EOR procedures are dependent on several factors such as: habitat of the residual oil, fluid properties, reservoir conditions, reservoir geometry, reservoir heterogeneity and the impact of the *in situ* stress regime. These factors are diverse in nature and each necessitates separate methodologies and techniques for their evaluation. However, resistivity image log data can be used as a fundamental framework for assessing several of these influencing parameters. This paper documents the use of resistivity images logs acquired from two wells within the Field A to make critical observations with respect to three of these factors and contribute to the overall design of the planned EOR operations.

Reservoir Geometry. Reservoir geometry is key to successful infill drilling across a field where there still remains significant uncertainty regarding the distribution of the reservoir sands.

Field A is located proximally to the main Cooper Basin depocentres and significant variations are observed in Tirrawarra Sandstone net reservoir thickness across the field (up to 87% variation from the field average). The Tirrawarra Sandstone is a fine to coarse grained sublitharenite deposited within a fluvial braided-stream environment with local conglomerate channels deposited in a waning-glacial environment. Locating likely depositional fairways is therefore a key priority. Uncertainty on depth/closure, pool contacts and variations in reservoir thickness have greatest bearing on *in place* at Field A and thus recovery estimates.

The uncertainty surrounding the geometry of the Field A reservoir can be reduced with the aid of resistivity image log data. Identification of sedimentological structures and bedding surfaces within these logs can be used to define tectonic tilt which in turn can be used to back-rotate palaeocurrent indicators to define transport directions and depositional fairways.

Reservoir Heterogeneity. Heterogeneity exists at all scales within a reservoir and can impact significantly on EOR operations such as: controlling the magnitude and nature of well connectivity, dictating reservoir compartmentalisation and influencing the balance of capillary, viscous and gravity

forces¹. This study utilises image logs to evaluate meso to mega scale sedimentary and structural features such as primary bedding surfaces, cross-beds and natural fractures. The orientation of sedimentary features directly affects permeability trends due to grain orientation and facies stacking². Natural fractures may be cemented and acting as fluid baffles or open and hydraulically conductive. Fracture permeability is also intrinsically linked to the *in situ* stress environment and will be addressed in this context.

Impact of *In situ* Stress. The orientation of the horizontal principal stresses are given by the orientation of borehole breakouts and drilling-induced tensile fractures commonly seen on borehole image logs. In vertical wells, the long axis of breakouts is oriented in the σ_{hmin} direction, and drilling-induced tensile fractures strike in the σ_{Hmax} direction. These observations are used in conjunction with other well data to constrain the *in situ* stress magnitudes and define the *in situ* stress regime. The *in situ* stress regime can then be used to assess several aspects of EOR operations that are dependent on the contemporary environment such as: preferential fluid flow directions, susceptibility of fracture populations to fluid flow and well placement to maximise drainage efficiency.

The remainder of this paper documents the application of the Field A image data to the numerous EOR related applications described above. The image log data were interpreted to catalogue: tectonic tilt; palaeocurrent indicators; *in situ* stress indicators, and; natural fracture populations. These data in turn are used to: constrain reservoir geometry; evaluate the impact of sedimentary structures and natural fractures on reservoir heterogeneity, and; use *in situ* stress to identify preferential fluid flow directions, the impact of natural fracturing and to propose an efficient injector-producer drilling pattern for EOR.

Image Log Data

Two image logs totalling 2297 ft of STAR resistivity image log data was acquired from Well A and Well B. These intervals stratigraphically cover the reservoir sands of the Tirrawarra Sandstone while also encompassing additional sediments above and below to facilitate accurate evaluation of tectonic tilt and *in situ* stress features (Fig. 2).

Image log quality directly affects the ability to successfully interpret *in situ* stress and geological features and artefacts generated during image acquisition and processing can also lead to misinterpretation. Image log quality was considered to be good in both Well A and Well B, however, intermittent processing artifacts did reduce the quality of image in Well A to poor over several small intervals. The quality of the images was not considered to compromise the integrity of the interpretation for this study.

Dip Classification Scheme

Sedimentological, structural and *in situ* stress features were interpreted from the STAR resistivity image logs and a classification scheme that incorporated these diverse surface types was required. The scheme consists of five sedimentological surface classifications that distinguish between primary bedding surfaces (PBSurf), low and high

quality current bedding (CBlow and CBhigh) and low and high quality unconformable boundaries (UBlow, UBhigh). Descriptions of each of these dip types and their sedimentological interpretation is given in

Table 1. Natural fractures are observed on resistive image logs as either conductive or resistive relative to the surrounding borehole. Therefore fractures were identified as either conductive (Cfrac) or resistive (Rfrac). Where displacement across a natural fracture could be identified the surface was classified as either a resistive or conductive fault (Rfault or Cfault). Each surface identified as either a fracture or fault was given a numerical subscript defined by the borehole coverage of the feature i.e observed on two pads, three pads, four pads, five pads or six pads. This classification scheme promotes unbiased interpretation and permits the distinction between observation and interpretation i.e nature of fracture versus genetic origin.

Tectonic Tilt

Prior to delineating accurate palaeocurrent directions, tectonic rotation of sediments post-deposition must be removed. This is achieved by identifying those sediments assumed to have been horizontal at their time of deposition. Such surfaces are predominantly conformable laminae within shale and heterolithic sequences. These surfaces were identified from the STAR resistivity image logs and classified as principal bedding surfaces (PBSurf).

Tectonic tilt is determined from PBSurf populations by observing depth intervals with consistent dip orientations. These intervals are termed ‘structural zones’. The top and base of a structural zone may correspond with significant unconformities or faults. The mean orientations of the primary bedding surfaces are determined for each structural zone and the mean orientation is used to back rotate palaeocurrent surfaces to their original depositional position.

Structural zones are best identified using dip walkout plots. These figures plot each PBSurf measurement as a vector in the direction the plane is dipping, starting with the deepest and finishing with the shallowest. Abrupt changes in dip direction are easily identified visually and interpreted as structural zones. Where sediments have not undergone a tectonic rotation post deposition, walkout plots appear as ‘scribble’ indicating no preferred orientation. Walkout plots may also be normalised such that the length of the vector for any measurement is relative to the dip magnitude of the sedimentary plane. Therefore, the effect of horizontal surfaces can be ignored relative to the inclined surfaces (large dip magnitudes).

Well A. Four hundred and sixty primary bedding surfaces were identified within Well A and their distribution is presented in Fig. 3. Analysis of the normalised dip walkout plots revealed thirteen structural zones were required to rotate primary bedding surfaces back to horizontal (Table 2 and Fig. 4). Significantly, only three zones were identified to have mean dip magnitudes greater than 5° indicating that these sediments have not been considerably affected by tectonic rotation post deposition. The greatest dip magnitudes were observed in the vicinity of faults within the Merrimelia

Formation at approximately 9481 ft and within the Murteree Shale (Zone 2).

Well B. Four hundred and twenty-nine primary bedding surfaces were identified within Well B and their distribution is presented in **Fig. 5**. Primary bedding surfaces observed within Well B presented a much more consistent orientation. The normalised dip walkout plot indicates a preferred orientation towards the northeast (**Fig. 6**). Two structural zones were identified at Well B. Zone 1 is characteristic of relatively flat lying sediments within the Merrimelia Formation, Tirrawarra Sandstone and lower Patchawarra sediments i.e. scribble like nature of walkout plots. Zone 2 however, is characterised by a dominant northeast orientation observed within the younger Patchawarra sediments, Murteree Shale, Toolachee Formation and Nappamerri Group sediments. Dip magnitudes are consistently less than 5° also indicating only minor post depositional tectonic tilt (**Table 3**).

Palaeocurrent Analysis

Palaeocurrent transport direction is inferred from the dip azimuth of high and low confidence current bedding surfaces, which are interpreted as cross-bedding foreset surfaces. Consequently, palaeo-flow is interpreted to have been parallel to the dip azimuth of the cross-bedding foreset surfaces at the time of deposition. High confidence trough and planar-tabular cross-bedding identifiable on more than three pads and/or flaps is considered the most reliable palaeo-current indicator, (CBhigh).

Current beds within fluvial bar forms are commonly associated with erosive bounding surfaces that are generally interpreted as fluvial accretion surfaces. The relationship of the dip azimuth of the accretion surfaces and the dip azimuth of the associated palaeo-current surfaces may help to distinguish lateral accretion bar forms from other kinds of fluvial bar forms.

Nappamerri Group. Forty seven palaeocurrent surfaces were identified within the sand units of the Nappamerri Group imaged at Well A compared with six at Well B. Transport direction at Well A is approximately to the east and to the southeast in Well B (**Fig. 7**).

Toolachee Formation. Toolachee Formation palaeocurrent indicators differ between Well A and Well B (**Fig. 7**). The dominant, transport direction at Well A is to the northwest at the base of the formation, briefly flowing to the west before flipping to the southeast, south and northeast in the youngest sediments. Transport direction at the base of the Toolachee Formation in Well B is also to the northwest and, flips to the southeast and to the northeast in the youngest sediments. Although mean orientations from Well A and Well B for the Toolachee Formation are considerably different (4° -> 171° N and 11° -> 025° N respectively) they are based on different sized populations (44 surfaces versus 19) and the walkout plots illustrate similar trends when looking at individual flow components.

Patchawarra Formation. Rotated palaeocurrent data within the Patchawarra Formation at Well A and Well B indicate transport directions to the south (**Fig. 7**). In both wells the sediments at the base of the Patchawarra do not show a preferred transport direction i.e. scribble like character on walkout plots. However, younger sediments clearly indicate a broadly southerly transport direction.

Tirrawarra Sandstone. Transport directions identified within the Tirrawarra Sandstone are very consistent between Well A and Well B (**Fig. 7**). Both indicate mean palaeocurrent directions to the northeast (039° N). The flow directions observed in the Tirrawarra Sandstone are consistent with the north-easterly strike of the Field A structure (**Fig. 1**).

Merrimelia Formation. Sands within the Merrimelia Formation show palaeocurrent indicators consistent with a southerly sediment transport direction in both Well A and Well B similar to directions observed within the Patchawarra Formation.

Discussion. The sediment transport directions interpreted from current data observed in Well A and Well B are relatively consistent between wells. There also appears to be several reversals in flow direction between and within individual formations. The dominant flow direction through time over the study interval is to the south. This is consistent with the location of Field A being proximal to, and toward the northern margin of, the main Cooper Basin depocentres.

In contrast however, transport direction within the Tirrawarra Sandstone is clearly to the northeast along the strike of the Field A structure (**Fig. 1**). This noticeable correlation of structure with sediment transport suggests a likely syn-depositional influence of structure trend on the type and amount of Tirrawarra Sandstone sediment deposited locally. This reduces uncertainty on the trend of reservoir facies with depositional margins likely to the northwest and southeast of this channelised braided fluvial environment.

There are also indications of transitional episodes where transport to the northeast and to the south occur within the same formation such as the Toolachee Formation. This is consistent with the preservation of depositional cyclicity within low-energy, fluvial units of this kind.

Diagenesis of the reservoirs at Field A is such that original sedimentary fabric is a key to porosity and permeability preservation. Sedimentary trends are also therefore critical to models for reservoir drainage and sweep. Identification of sediment transport direction to the northeast in the Tirrawarra Sandstone directs tighter well spacing with sweep preferential to the northeast-southwest direction.

In situ Stress Tensor

Assuming the vertical stress is a principal stress, the in-situ stress tensor is comprised of five separate elements which are: pore pressure; vertical stress magnitude; minimum horizontal stress magnitude; maximum horizontal stress orientation, and; maximum horizontal stress magnitude. These five elements were evaluated for the Field A area using an eclectic collection of data from Well A and Well B.

Pore pressure was estimated from formation multi tester measurements in Wells A & B. These measurements showed significant variation and consequently, several pore pressure cases are possible (**Fig. 8**). A conservative estimate utilizing a pore pressure gradient of 0.442 psi/ft (10.0 MPa/km) has been used for all the stress related calculations herein.

The vertical stress magnitude is calculated from a density log curve by integrating the density values multiplied by the acceleration due to gravity and the sample spacing. The length of the density logging run was considerably greater in Well A compared to Well B and therefore the vertical stress magnitude was calculated using the density log acquired at Well A (**Fig. 8**).

The minimum horizontal stress magnitude was estimated by averaging two leak-off tests conducted in Well A & B (**Fig. 8**).

The maximum horizontal stress orientation was determined from the observation of borehole breakouts and drilling induced tensile fractures within Well A and Well B (**Figs. 9 and 10**). A total of 166 breakouts and 3 drilling induced tensile fractures (DITFs) were observed with a total length of 371.2 and 2.2 ft respectively. Borehole breakouts consistently indicate a σ_{Hmax} of approximately 117°N (mean unweighted σ_{Hmax} orientation derived from borehole breakouts) and DITFs indicate a mean σ_{Hmax} orientation of 114°N.

A summary of mean σ_{Hmax} orientations derived from the interpretation are presented in

Table 6 and Table 7. Length-weighted azimuths are biased by long and deep breakouts respectively. Unweighted azimuths have been used for all fracture susceptibility calculations herein. These observations are consistent with other NE-SW stress indicators measured at Field A and adjacent areas (**Table 8**).

Frictional limits provide an upper bound to the maximum horizontal stress magnitude, above which faulting will occur. This method is effective in constraining σ_{Hmax} magnitude provided all other in-situ stress components are known. The maximum horizontal stress magnitude at Field A was constrained using the frictional limit methodology and the observation that drilling induced tensile fractures occur in conjunction with borehole breakout within the Merrimelia Formation in Well A and the Patchawarra Formation in Well B.

The occurrence of DITFs provides a lower bound to the maximum horizontal stress magnitude when assuming negligible tensile rock strength. Upper and lower bounds to the σ_{Hmax} magnitude were calculated for the pore pressure case considered using the following assumptions:

- Maximum σ_{Hmax} magnitude modelling uses a coefficient of friction of 0.6.
- Minimum σ_{Hmax} magnitude modelling based on the occurrence of DITF occurrence in Well A and Well B.
- σ_{hmin} magnitude is an average of pressure gradients estimated from 2 leak-off pressures obtained in Well A and Well B.
- σ_v magnitude is calculated by extrapolating density values from approx. ~9000 ft to the surface.

Stress modelling of the maximum horizontal stress tensor for the selected pressure case reveals a strike-slip stress regime where $\sigma_{hmin} < \sigma_v < \sigma_{Hmax}$ (**Fig. 11**).

Natural Fracture Distribution and Hydraulic Conductivity

The relationship between natural subsurface fluid flow and *in situ* stress is due to the focusing of fluid flow along planes suitably oriented to be tensile or shear fractures within the *in situ* stress field. Pre-existing natural fractures in these orientations tend to be open and transmit fluids. Hence, although pre-existing natural fractures may have a wide variety of orientations, those suitably oriented to be tensile or shear fractures within the *in situ* stress field tend to be open and hydraulically conductive.

Here we observe the relationship between resistive and conductive fracture populations observed from the resistivity image logs with fracture susceptibility models predicted using the *in situ* stress tensor defined for Field A.

Fracture Distribution. Fractures were observed and classified from two resistivity image logs using the scheme defined in

Table 1. Fracture orientations are summarized in **Figs. 12 and 13** and raw and corrected fracture densities⁵ are presented in **Table 9 and Table 10**.

Conductive and resistive fractures predominantly dip 30-60° and strike in a dominant direction of approximately 065°N in both Well A and Well B. There also exist less dominant fracture strikes oriented approximately 015°N and 120°N. Stearns and Friedman⁶ describe the distribution of tensile, shear and thrust faults (low angle shear faults) and fractures related to the geometry of an anticlinal fold. The observed fracture trends across Field A correspond with fracture geometries expected to be associated with an anticlinal fold such as the primary structure of the NE-SW trending Field A (**Fig. 1**). Given the orientation of the field structure, the 065°N fracture trend would correspond with thrust (approx. 30° dip) fractures and the 015°N and 120°N fracture trends would correspond with shear fractures (approx. 60° dip). Rose plots of fracture subsets associated with displacement correspond with orientations predicted for shear and thrust faults and fractures (**Fig. 14**).

It is also evident that there is significantly greater fracturing observed at Well A relative to Well B. Corrected fracture densities at Well A are nearly an order of magnitude greater than those observed at Well B and this may be attributed to the more crestal location of Well A relative to Well B (**Fig. 1**).

Fracture densities also vary with respect to stratigraphy within individual wells (**Table 9 and Table 10**). The most significant observation is that corrected fracture densities are greatest from the Murteree Shale down to the Merrimelia Formation. The Tirrawarra Sandstone reservoir contains fracture densities up to 0.79 conductive fractures per meter (Well A) and is almost unaffected by resistive fractures (only one observed fracture). The occurrence of conductive fractures within the reservoir unit implies that they can enhance flooding operations given favourable *in situ* stress

conditions and well pattern design. The lack of resistive fractures implies that it is unlikely that permeability will be affected by structural baffles.

Fracture Susceptibility. The relationship between natural subsurface fluid flow and *in situ* stress is due to the focusing of fluid flow along planes suitably oriented to be tensile or shear fractures within the *in situ* stress field. Pre-existing natural fractures in these orientations tend to be open and transmit fluids. Hence, although pre-existing natural fractures may have a wide variety of orientations, those suitably oriented to be tensile or shear fractures within the *in situ* stress field tend to be open and hydraulically conductive.

Fracture susceptibility models are generated using the *in situ* stress field to identify what are the critical fracture orientations or, which orientations are most susceptible to the *in situ* stress environment. They are plotted as stereonets which are contoured relative to the pressure change (ΔP) required to initiate failure. All points are plotted as poles to planes using a southern hemisphere projection. Susceptibilities of fracture initiation orientations may also be considered and are dependent on using the material properties of the host rock rather than the strength of a pre-existing discontinuity. For further information regarding this technique see Mildren et al.⁷.

Fig. 15 illustrates a fracture susceptibility model generated for Field A within the Tirrawarra Sandstone reservoir. Fracture orientations with the greatest susceptibility are those dipping greater than approximately 30° and striking between either 060°N and 105°N or 125°N and 170°N. These critical orientations also represent the preferential orientations of any new fractures that flooding may initiate. The majority of observed fractures strike within these orientations and dip greater than 30°.

Given that these calculations are made for reservoir conditions, flooding operations will increase pore pressure and drive failure of these pre-existing fractures to enhance permeability, predominantly in the WNW-ESE and NNW-SSE orientations.

EOR Drilling Pattern

Reservoir drainage is anisotropic and sensitive to the *in situ* stress field, even in reservoirs not subject to fracture stimulation, perhaps because of stress-sensitive natural fractures and/or micro-fractures. Again the recognition of such can help optimise plans for field development.

Fractures induced by reservoir flooding may be responsible for the observed directionality of reservoir floods and well pair rate correlations. Fracture networks composed of shear, tensile and mixed-mode fractures (extensional-shear) propagate in the plane of the σ_1 and σ_2 principal stress directions hydraulic conductivity is maximised in the direction of σ_2 ⁸. In order to maximise sweep efficiency in flooding operations, injector-producer pairs should not be aligned in the principal flow direction (σ_1 - σ_2 plane). If injector-producer pairs are so aligned, injected fluids will flow directly from the injector to the producer, bypassing much of the reservoir. If injectors are aligned, flooding fluids from the injectors rapidly link up, forming a 'curtain' that sweeps hydrocarbons to

producing wells, which should be offset from the injectors in the σ_3 direction.

At Field A in the Cooper Basin, the intermediate principal stress (σ_2) is the vertical stress and therefore the best flow direction would primarily be vertical and in the direction of σ_{Hmax} (117°N). However, this study has also identified two other permeability conduits that may impact on flooding operations. Palaeocurrent indicators reveal that sediment transport within the Tirrawarra Sandstone was dominantly towards 030°N and it has been documented that permeability is maximized within units parallel to palaeocurrent directions². Fracture characterisation and fracture susceptibility models suggest that the dominant pre-existing fracture trend oriented approximately 065°N is critically oriented for fluid flow and may dominate stress related fracture networks.

Given three permeability anisotropies that promote fluid flow in three separate directions, an EOR drill pattern can still be designed that will permit a successful flood if any one anisotropy dominates the operation. Although the relative efficiency of these permeability trends remains unknown, an optimal well pattern can be proposed that would maximize flooding efficiency prior to any production data. We propose an east-west oriented well array within the Tirrawarra Sandstone of Field A that promotes connectivity utilising sedimentological, natural fracture and the *in situ* stress related permeability (**Fig. 16**). As production data becomes available, relative permeabilities can be evaluated and modifications to the drill pattern can be made.

Conclusions

Image log tools are expensive to run and are not always implemented on a routine basis. However, this study has showcased the usefulness of image logs to derive sedimentological, structural and *in situ* stress data with benefit to planning EOR operations. Three distinct permeability trends were highlighted at Field A, and although their relative efficiencies remain untested significant constraint can be placed on the design to enhance flooding operations.

References

1. Henson, R., Todd, A., & Corbett, P. "Geologically Based Screening Criteria for Improved Oil Recovery Projects", SPE 75148, SPE/DOE Improved Oil Recovery Symposium, 13-17 April, Tulsa, Oklahoma (2002).
2. Evans, R. C., "An Investigation Into the Influence of Common Sedimentary Structures and Diagenesis on Permeability Heterogeneity and Anisotropy in Selected Sands and Sandstones", SPE 17130, (1987).
3. Zoback, M. L., "First and second-order patterns of stress in the lithosphere: The World Stress Map Project", *J. Geophys. Res.*, 97, B8, (1992), p11703-11728.
4. Chandler, E., "Pressure Constraints with Respect to Fault Seal Integrity and Reservoir Flooding in the Patchawarra Trough, Cooper Basin", Unpubl honours thesis, University of Adelaide, (2003).

5. Terzaghi, R.D., “Sources of error in joint surveys”, *Geotechnique*, V.15., (1965), p287-304.
6. Stearns, D.W. & Friedman, M. “Reservoirs in Fractured Rock” *AAPG Memoir* 16, (1972), pp.82-100.
7. Mildren, S.D., Hillis, R.R., Dewhurst, D.N., Lyon, P.J., Meyer, J.J. & Boulton, P.J., “FAST (Fault Seal Analysis Technology): A new technique for geomechanical assessment of the risk of reactivation-related breach of fault seals”, *AAPG Hedberg* Volume 1, (in press).
8. Sibson, R. H., “Structural permeability of fluid-driven fault-fracture meshes”, *Journal of Structural Geology*, v. 18, (1996), p1031-1042.
9. Bell, J. S., “Investigating stress regimes in sedimentary basins using information from oil industry wireline logs and drilling records”, In: Hurst, A., Lovell, M. A. and Morton, A. C. (eds.). *Geological Applications of Wireline Logs*, Geological Society of London, Special Publication 48, (1990), p305-325.

Acknowledgements

The authors would like to acknowledge Santos Ltd and all joint venture partners associated with Field A for permission to publish this paper.

Nomenclature

σ_{Hmax}	=	<i>Maximum horizontal stress</i>
σ_{Hmin}	=	<i>Minimum horizontal stress</i>
σ_v	=	<i>Vertical stress</i>
σ_1	=	<i>Principal in situ stress</i>
σ_2	=	<i>Intermediate principal stress</i>
σ_3	=	<i>Minimum principal stress</i>
ΔP	=	<i>Pressure increase required to initiate failure</i>

Surface Classification	Full Name	Description	Interpretation	Dip Magnitude	Symbols
PBSurf	Principal conformable bedding surface	Horizontal planar bedding surface commonly within shale or heterolithic. Defines palaeo-horizontal.	May represent laminae, conformable bed boundaries or planar stratification surfaces.	<10°	Blue circle tadpole, blue sinusoid
CBlow	Current bedding, low quality (≤3 pads)	Sandstone with generally intermediate dip magnitudes bounded by erosive surfaces. Systematic decrease in dip magnitude up section. Planar and non-planar surfaces.	Boundaries of cross-bed cosets, reliable palaeocurrent indicators and associated with either planar tabular cross-bedding or trough cross-bedding.	15°-35°	Light green circle tadpole, light green sinusoid
CBhigh	Current bedding, high quality (>3 pads)	Same as CBlow but higher quality interpretation.	Same as CBlow.	15°-35°	Dark green circle tadpole, dark green sinusoid
UBlow	Unconformable bedding, low quality (≤3 pads)	Erosive bedding surface on greater than 3 pads, visibly truncates other surfaces	Erosive sedimentological surface that may include: erosive bed boundary, accretion surface or reactivation surfaces.	<15°	Orange circle tadpole, orange sinusoid
UBhigh	Unconformable bedding, high quality (>3 pads)	Same as UBlow but higher quality interpretation	Same as UBlow.	<15°	Red circle tadpole, red sinusoid
Cfrac	Conductive fracture	High angle, planar, conductive surface visible on 2-6 pads (denoted by subscript).	Fracture surface cross-cutting the borehole in filled with drilling fluid. Possibly open away from wellbore.	>30°	Light blue triangle tadpole, light blue sinusoid
Cfault	Conductive fracture with obvious displacement	High angle, planar, conductive surface visible on 2-6 pads (denoted by subscript) and associated with obvious displacement and higher surrounding fracture density	Fault surface in filled with drilling fluid. Possibly hydraulically conductive away from wellbore.	>30°	Light blue diamond tadpole, mustard sinusoid
Rfrac	Resistive fracture	High angle, planar, resistive surface visible on 2-6 pads (denoted by subscript).	Cemented fracture surface cross-cutting the borehole. Possibly a baffle to fluid flow.	>30°	Mustard triangle tadpole, light blue sinusoid
Rfault	Resistive fracture with obvious displacement	High angle, planar, resistive surface visible on 2-6 pads (denoted by subscript) and associated with obvious displacement and higher surrounding fracture density	Cemented (healed) fault surface. Possibly acting as a baffle to fluid flow.	>30°	Mustard diamond tadpole, mustard sinusoid

Table 1 Dip classification scheme utilised in the interpretation of Field A STAR resistivity image logs.

Formation	Zone	Depth Interval		PBsurf Mean		
		Top (ft)	Bottom (ft)	Dip	Direction	Number
All	All	8501	9599	1.6	119	460
Nappamerri Gp	Zone13	7948	8588	0.8	358	44
Toolachee Fm	All	8588	8694	1.7	310	20
	Zone12	8587	8620	3.4	034	9
	Zone11	8620	8693	3.9	265	11
Murteree Fm	All	8693	8730	22.6	092	37
	Zone10	8693	8711	29.6	092	28
	Zone9	8711	8730	1.1	125	9
Patchawarra Fm	All	8730	9405	0.3	224	279
	Zone8	8730	8850	1.0	059	48
	Zone7	8850	9075	1.9	210	31
	Zone6	9075	9240	0.5	231	97
	Zone5	9240	9410	0.3	263	103
Patch-Tirra	Zone4	9405	9446	5.8	116	7
Tirrawarra Sst	Zone3	9446	9470	4.7	160	15
Merrimelia Fm	All	9470	9842	4.7	212	58
	Zone2	9470	9490	12.9	181	11
	Zone1	9490	9600	2.6	026	45

Table 2 Summary of tectonic tilt with respect to stratigraphy and structural zones from Well A.

Formation	Zone	Depth Interval		PBsurf Mean		
		Top (ft)	Bottom (ft)	Dip	Direction	Number
All		7909	9730	1.5	048	502
Nappamerri Gp	All	7909	8638	2.0	055	54
Toolachee Fm	All	8638	8754	1.8	357	15
Murteree Shale	All	8754	8800	2.8	069	20
Patchawarra Fm	All	8800	9502	1.7	047	351
Patch-Tirr	All	9502	9548	1.0	002	18
Tirrawarra Sst	All	9548	9590	4.1	268	16
Merrimelia Fm	All	9590	9730	1.7	121	28
	Zone 2	8500	9404	2.3	039	355
	Zone 1	9404	9730	0.8	152	147

Table 3 Summary of tectonic tilt with respect to stratigraphy and structural zones for Well B.

Formation	Depth Interval		CBlow & CBhigh Mean			UBlow & UBhigh Mean		
	Top (ft)	Bottom (ft)	No.	Dip	Direction	No.	Dip	Direction
Nappamerri Gp	7948	8588	47	10.2	076	14	0.9	229
Toolachee Fm	8588	8694	44	4.3	171	13	0.8	156
Murteree Fm	8693	8730	7	4.4	279	4	24.0	262
Patchawarra Fm	8730	9405	382	2.9	151	107	0.5	343
Patch-Tirra	9405	9446	49	16.4	179	28	6.3	339
Tirrawarra Sst	9446	9470	26	12.9	039	14	3.9	017
Merrimelia Fm	9470	9842	33	9.4	177	14	1.9	349

Table 4 Mean palaeocurrent orientations interpreted from Well A STAR resistivity image log. These data have been rotated for tectonic tilt.

Formation	Depth Interval		CBlow & CBhigh Mean			UBlow & UBhigh Mean		
	Top (ft)	Bottom (ft)	No.	Dip	Direction	No.	Dip	Direction
Nappamerri Gp	7909	8638	6	17.0	199	2	3.2	180
Toolachee Fm	8638	8754	19	10.6	025	4	4.3	347
Murteree Shale	8754	8800	0	-	-	0	-	-
Patchawarra Fm	8800	9502	159	5.2	172	53	3.6	056
Patch-Tirr	9502	9548	16	3.5	311	11	1.2	292
Tirrawarra Sst	9548	9590	29	16.2	039	6	4.6	342
Merrimelia Fm	9590	9730	31	10.0	150	9	6.6	019

Table 5 Mean palaeocurrent orientations interpreted from Well B STAR resistivity image log. These data have been rotated for tectonic tilt.

Well Name	Lat	Long	Log Type	Image Interval		Un-weighted				Length-weighted			
				Top (ft)	Bottom (ft)	N	Azi	SD	Q	L	Azi	SD	Q
Well A	-27.62	139.99	STAR	8500	9599	68	122	7.1	A	177.3	119	6.2	A
Well B	-27.59	140.00	STAR	8536	9734	98	114	6.3	A	193.9	114	5.4	A
Totals						166	117	7.7	A	371.2	117	6.4	A

Table 6 Breakout derived mean σ_{Hmax} orientations. Lat and Long are the latitude and longitude of the well locations, N is the total number and ΣL the total length (ft) of breakouts in the well. Azi and SD are the mean strike (000°-180°N) of breakout-derived σ_{Hmax} orientation in the well and the standard deviation in degrees as determined by directional statistics. Q is the quality rating of the measurement determined using the World Stress Map ranking system³.

Well Name	Lat	Long	Log Type	Image Interval		Un-weighted				Length-weighted			
				Top (ft)	Bottom (ft)	N	Azi	SD	Q	ΣL	Azi	SD	Q
Well A	-27.62	139.99	STAR	8500	9599	1	117.09	0	E	1.4	117.09	0	E
Well B	-27.59	140.00	STAR	8536	9734	2	111.94	4.164	D	0.8	111.38	4.126	D
Totals						3	113.67	4.178	D	2.2	115.05	3.688	D

Table 7 DITF derived mean σ_{Hmax} orientations. Lat and Long are the latitude and longitude of the well locations, N is the total number and ΣL the total length (ft) of DITF in the well. Azi and SD are the mean strike (000°-180°N) of DITF-derived σ_{Hmax} orientation in the well and the standard deviation in degrees as determined by directional statistics. Q is the quality rating of the measurement determined using the World Stress Map ranking system³.

Well Name	Lat	Long	Log Type	Image Interval		Un-weighted				Length-weighted			
				Top (ft)	Bottom (ft)	N	Azi	SD	Q	ΣL	Azi	SD	Q
Well C	-27.58	140.01	FMS	8822	9803	45	129	6	A	360.89	130	5	A
Well D	-27.65	139.94	FMS	8753	9678	126	126	8	A	123.69	126	7	A
Well E	-27.57	140.14	HDT	6257	7884	142	142	11	B	55.774	144	12	B
Well F	-27.59	140.12	HDT	-	-	152	152	-	D	13.123	152	-	D

Table 8 Extant breakout derived mean σ_{Hmax} orientations from Field A and adjacent regions⁴. Lat and Long are the latitude and longitude of the well locations, N is the total number and ΣL the total length (ft) of DITF in the well. Azi and SD are the mean strike (000°-180°N) of DITF-derived σ_{Hmax} orientation in the well and the standard deviation in degrees as determined by directional statistics. Q is the quality rating of the measurement determined using the World Stress Map ranking system³.

Formation				Conductive Fractures and Faults				Resistive Fractures and Faults			
				Raw Data		Corrected Data		Raw Data		Corrected Data	
Name	Top	Bottom	Thickness	No. Of Fracs	Density (fracs/m)	No. Of Fracs	Density (fracs/m)	No. Of Fracs	Density (fracs/m)	No. Of Fracs	Density (fracs/m)
Nappamerri Group	2590.80	2617.52	26.7	0	0.00	0.00	0.00	1	0.04	1.58	0.06
Toolachee Formation	2617.52	2649.82	32.3	4	0.12	6.11	0.19	0	0.00	0.00	0.00
Murteree Shale	2649.82	2660.90	11.1	7	0.63	12.40	1.12	5	0.45	8.71	0.79
Patchawarra Formation	2660.90	2879.33	218.4	69	0.32	103.09	0.47	13	0.06	19.03	0.09
Tirrawarra Sandstone	2879.33	2886.51	7.2	4	0.56	5.70	0.79	1	0.14	1.22	0.17
Merrimelia Formation	2886.50	2925.78	39.3	27	0.69	42.80	1.09	7	0.18	13.29	0.34

Table 9 Table summarising conductive and resistive fracture populations identified within STAR resistivity image logs from Well A.

Formation				Conductive Fractures and Faults				Resistive Fractures and Faults			
				Raw Data		Corrected Data		Raw Data		Corrected Data	
Name	Top	Bottom	Thickness	No. Of Fracs	Density (fracs/m)	No. Of Fracs	Density (fracs/m)	No. Of Fracs	Density (fracs/m)	No. Of Fracs	Density (fracs/m)
Nappamerri Group	2601.77	2617.52	15.7	0	0.00	0.00	0.00	3	0.19	4.12	0.26
Toolachee Formation	2617.52	2649.82	32.3	3	0.09	4.12	0.13	1	0.03	1.99	0.06
Murteree Shale	2649.82	2660.90	11.1	1	0.09	1.99	0.18	0	0.00	0.00	0.00
Patchawarra Formation	2660.90	2879.33	218.4	14	0.06	21.84	0.10	0	0.00	0.00	0.00
Tirrawarra Sandstone	2879.33	2886.51	7.2	1	0.14	1.37	0.19	0	0.00	0.00	0.00
Merrimelia Formation	2886.50	2966.92	80.4	7	0.09	13.04	0.16	6	0.07	11.32	0.14

Table 10 Table summarising conductive and resistive fracture populations identified within STAR resistivity image logs from Well B.

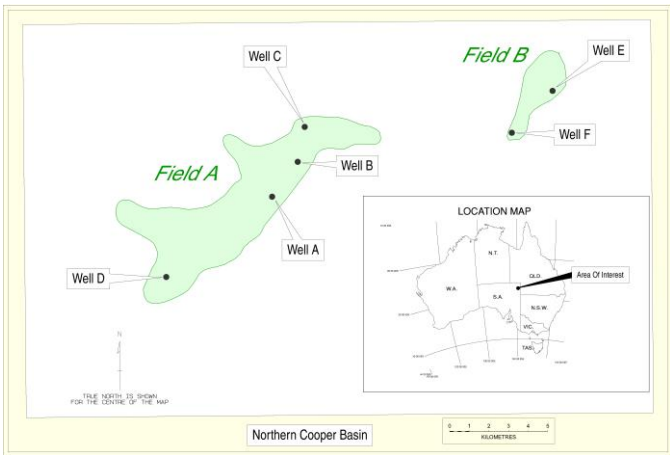


Figure 1 Field A location map within the Cooper Basin, Australia also illustrating the locations of Wells A to F.

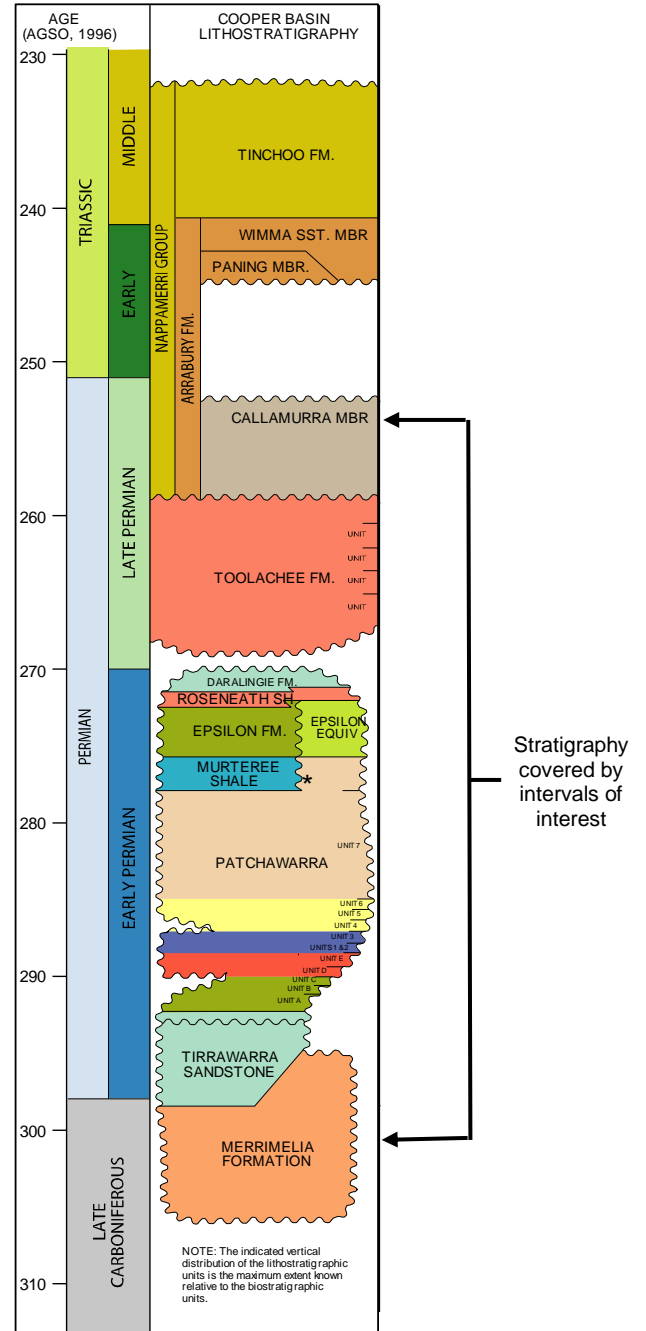


Figure 2 Partial stratigraphic column for the Cooper-Eromanga Basin. Coverage of image log intervals also indicated (Santos Ltd).

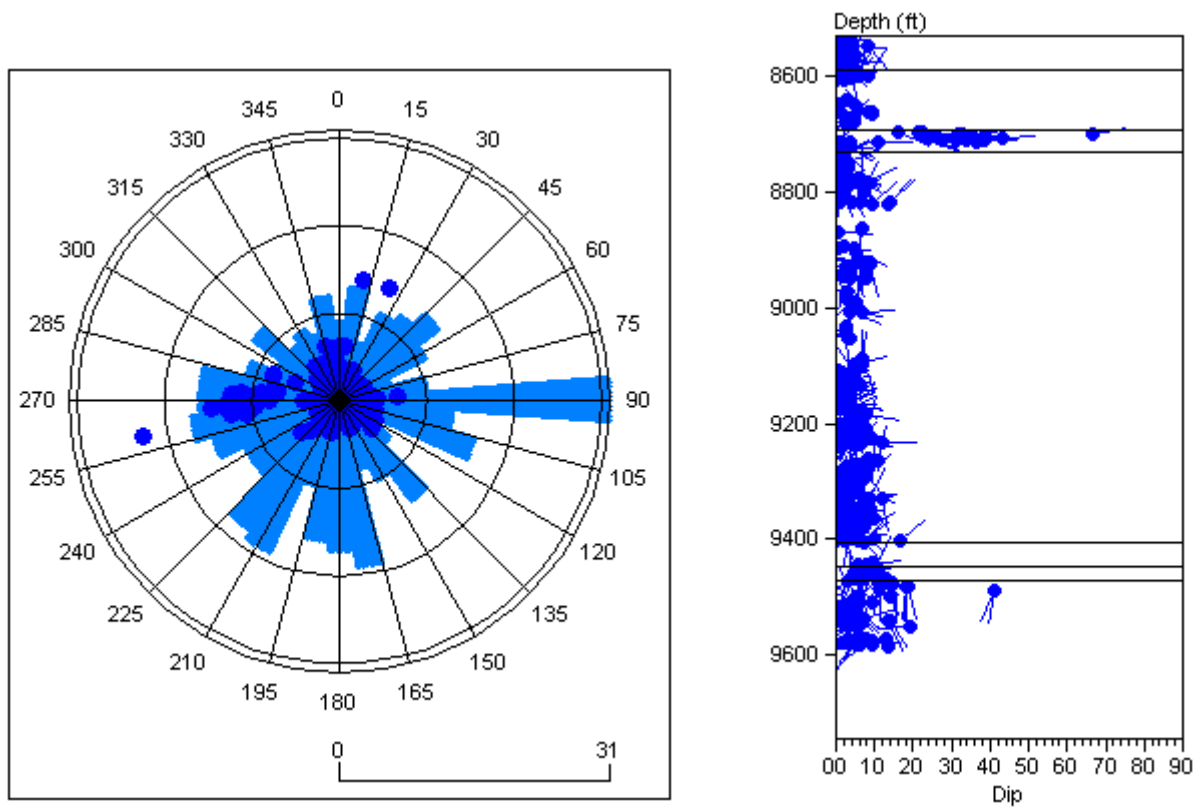


Figure 3 PBsurf distribution illustrated by rose, stereonet and depth plot for Well A. Surfaces are plotted as poles to planes (southern hemisphere projection) on stereonets.

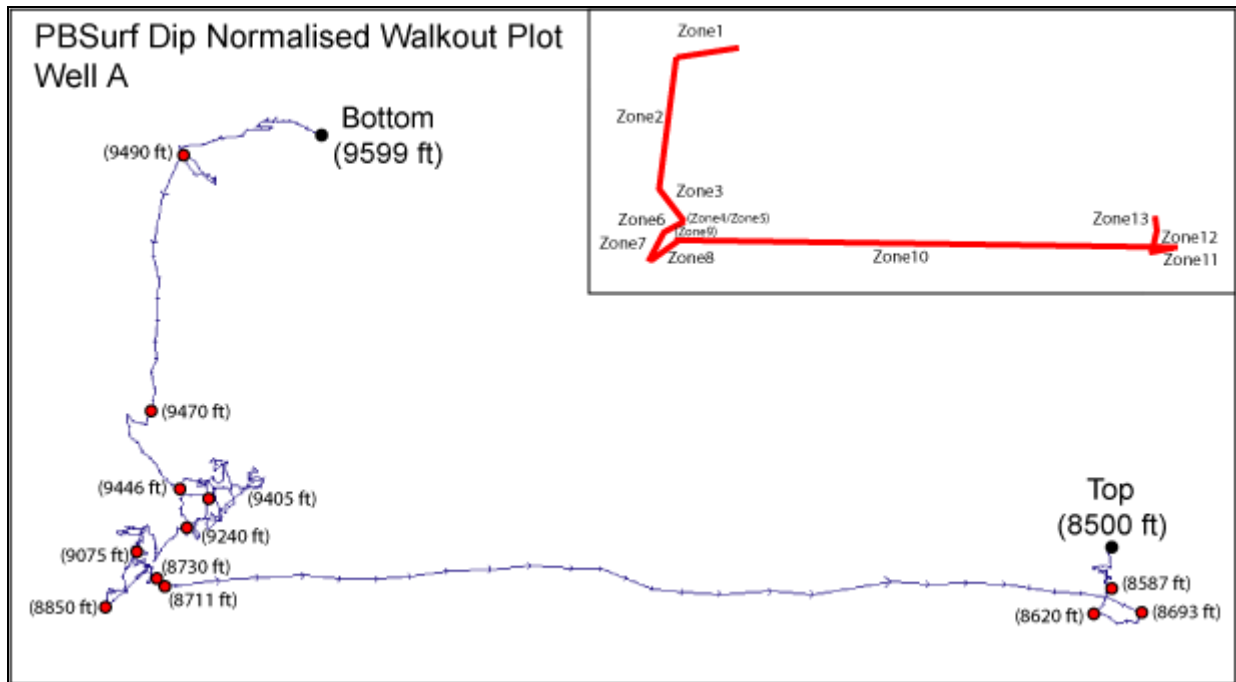


Figure 4 Dip normalised walkout plot illustrating zone intervals for Well A. Special surfaces also included.

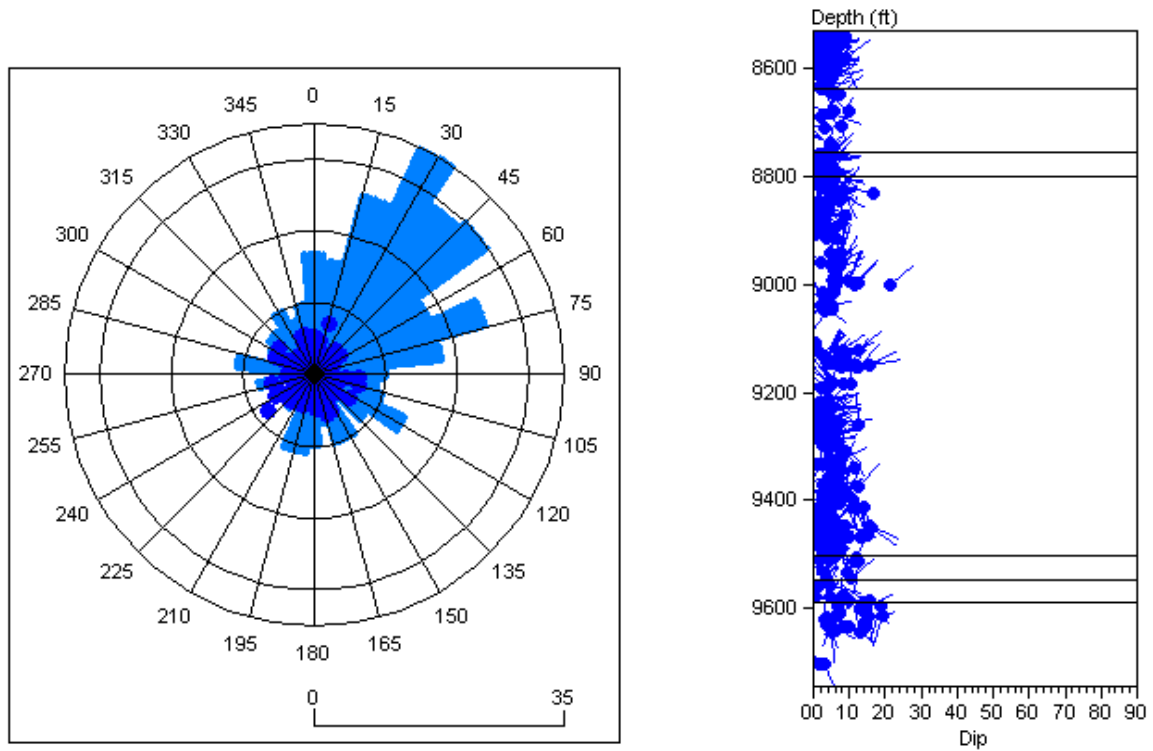


Figure 5 PBsurf distribution illustrated by rose, stereonet and depth plot for Well B. Surfaces are plotted as poles to planes (southern hemisphere projection) on stereonets.

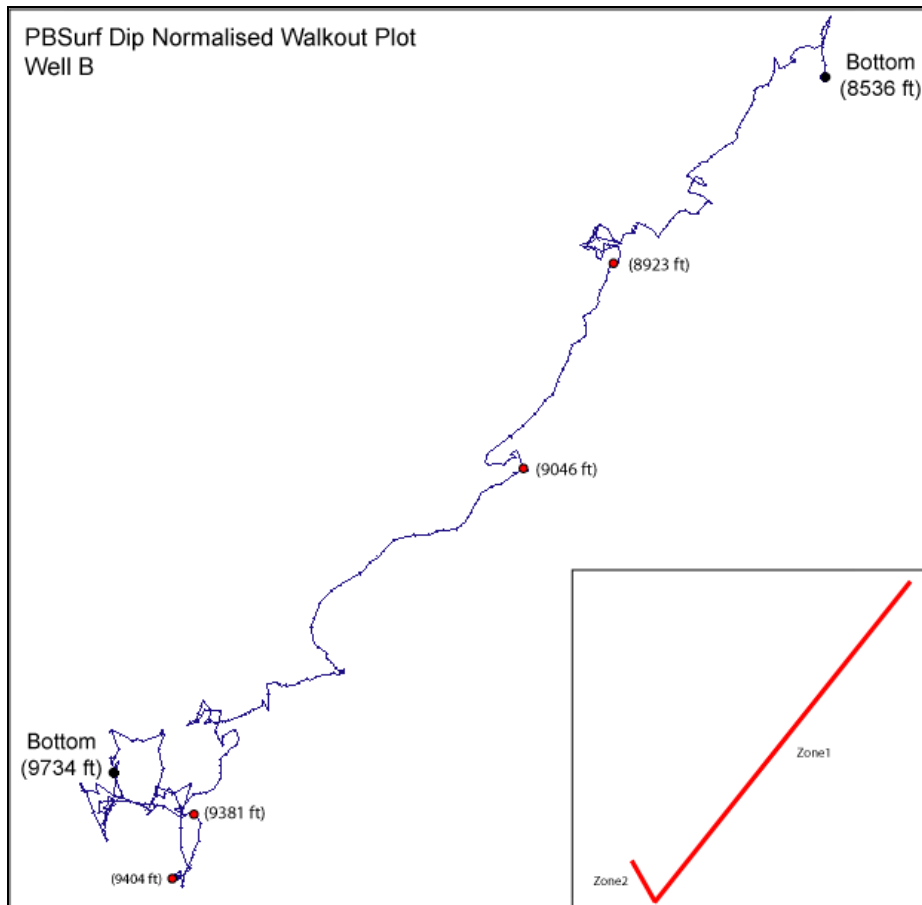


Figure 6 Dip Normalised walkout plot illustrating zone intervals for Well B.

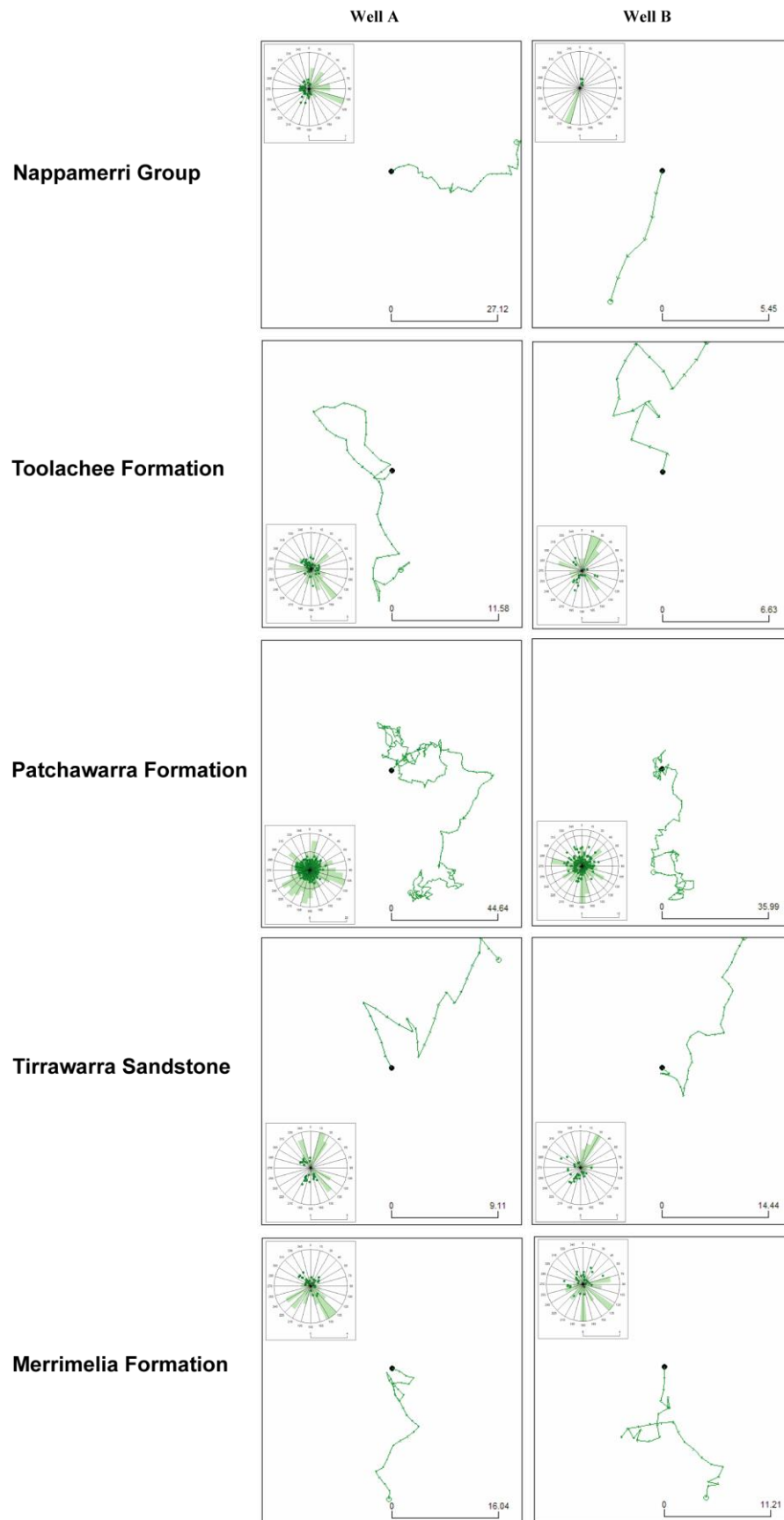


Figure 7 Comparison of palaeocurrent directions plotted as walkout plots interpreted from Well A and Well B with respect to stratigraphic units. Rose diagram of dip directions are superimposed with polar plots of dip/dip direction vectors and inset within each walkout plot.

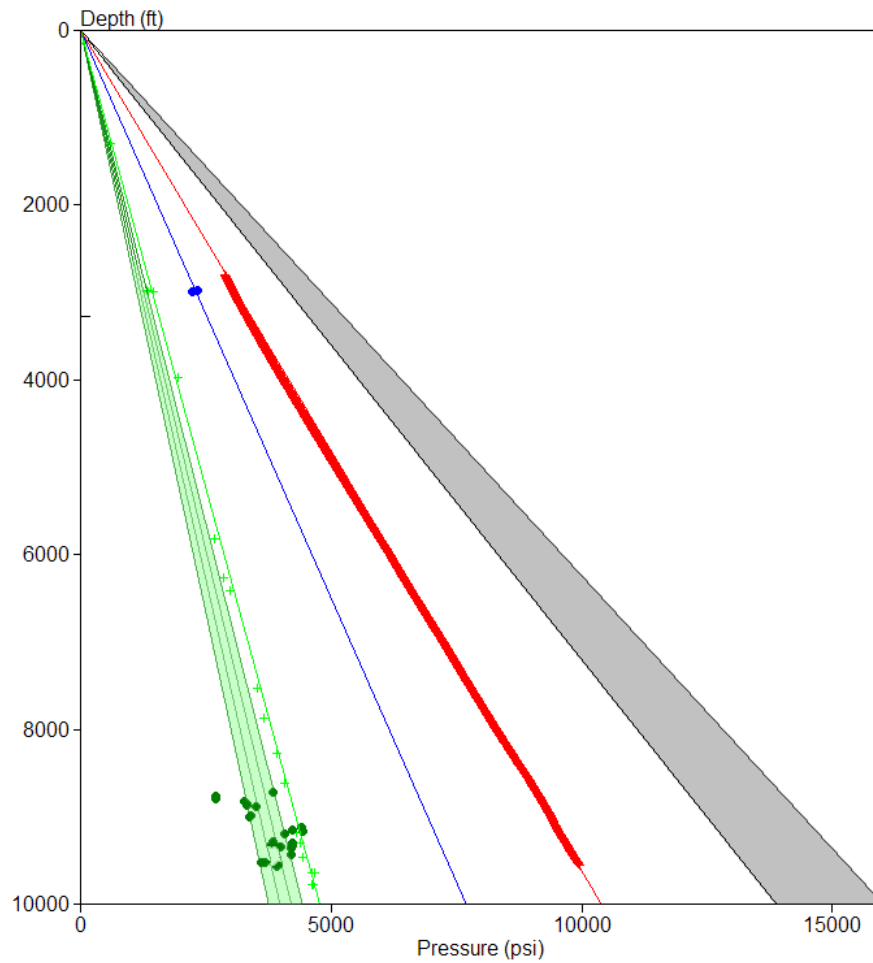


Figure 8 *In situ* stress magnitude profile with respect to depth generated for the Field A area where pore pressure measurements are dark green symbols, mudweight measurements are light green symbols, leak-off pressures are blue symbols and vertical stress measurements are red. Range of σ_{Hmax} values based on the four pore pressure cases is shown as the grey shaded area.

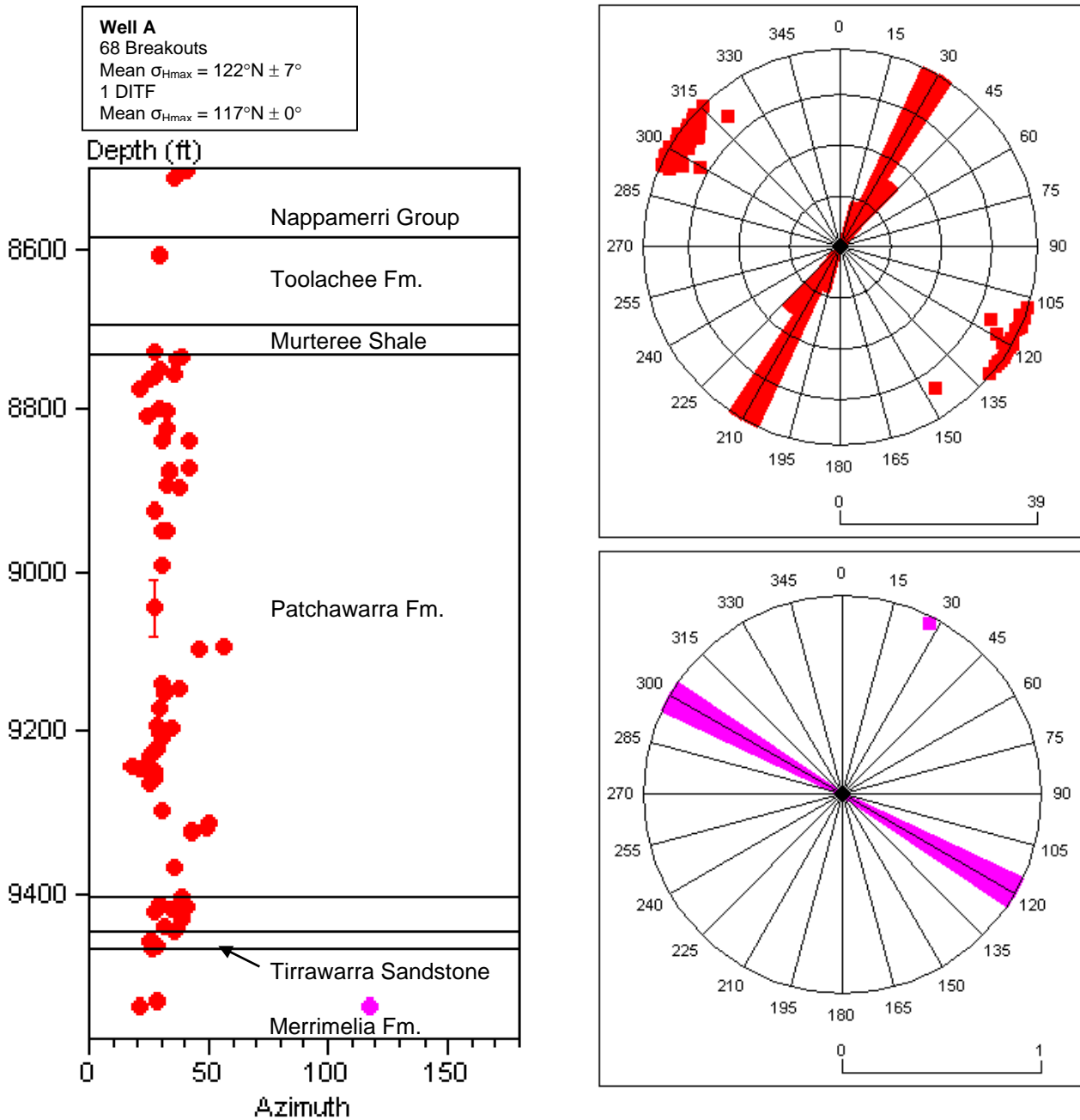


Figure 9 Orientation summary of borehole breakouts (red) and drilling induced tensile fractures (DITFs; purple) interpreted from the image log interval (8500-9599 ft) of Well A. a) Breakout data plotted as strike azimuths and poles to plane stereonet projection where scale represents the number of breakouts. b) DITF data plotted as strike azimuth and poles to plane stereonet projection where scale represents number of DITFs. c) Breakout and DITF strike azimuth depth interval plot.

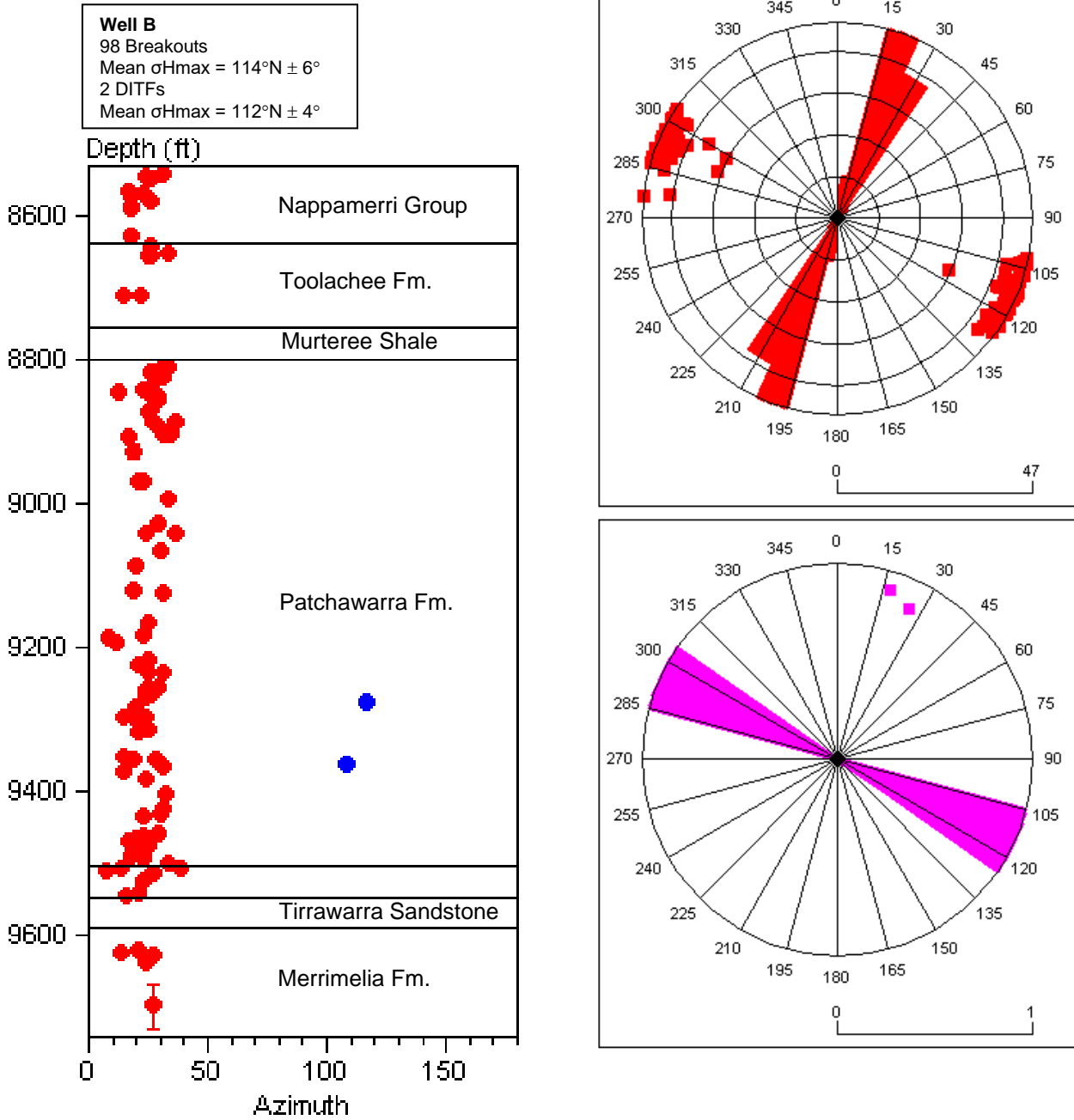


Figure 10 Orientation summary of borehole breakouts (red) and drilling induced tensile fractures (DITFs; purple) interpreted from the image log interval (8536-9734 ft) of Well B. a) Breakout data plotted as strike azimuths and poles to plane stereonet projection where scale represents the number of breakouts. b) DITF data plotted as strike azimuth and poles to plane stereonet projection where scale represents number of DITFs. c) Breakout and DITF strike azimuth depth interval plot.

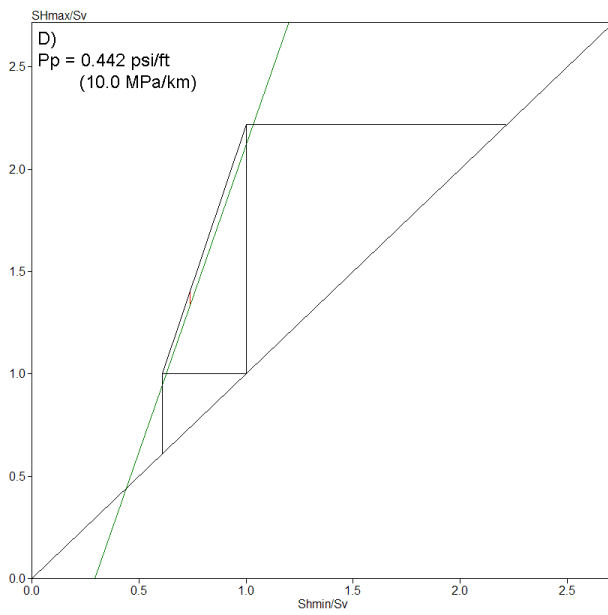
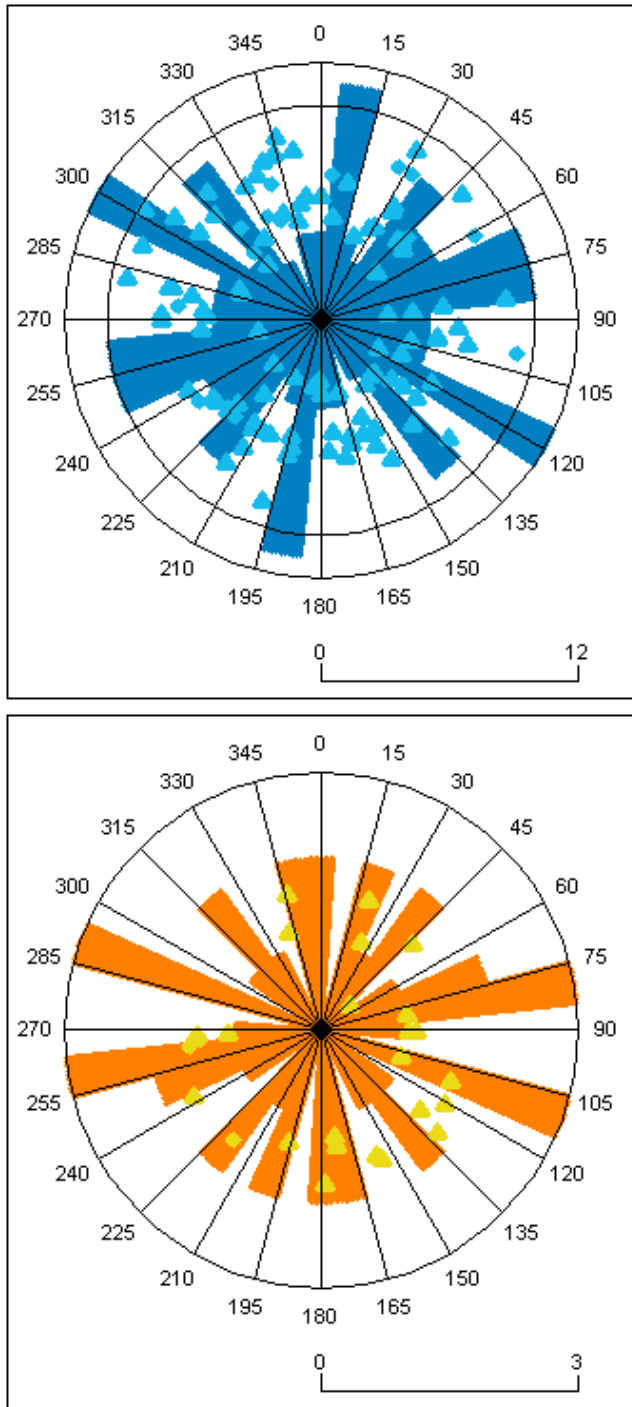


Figure 11 Constrained maximum horizontal stress magnitude regions calculated for the pore pressure case where $P_p = 0.442 \text{ psi/ft}$ (10.0 MPa/km).



Well A
 111 Conductive Fractures (blue)
 26 Resistive Fractures (orange)

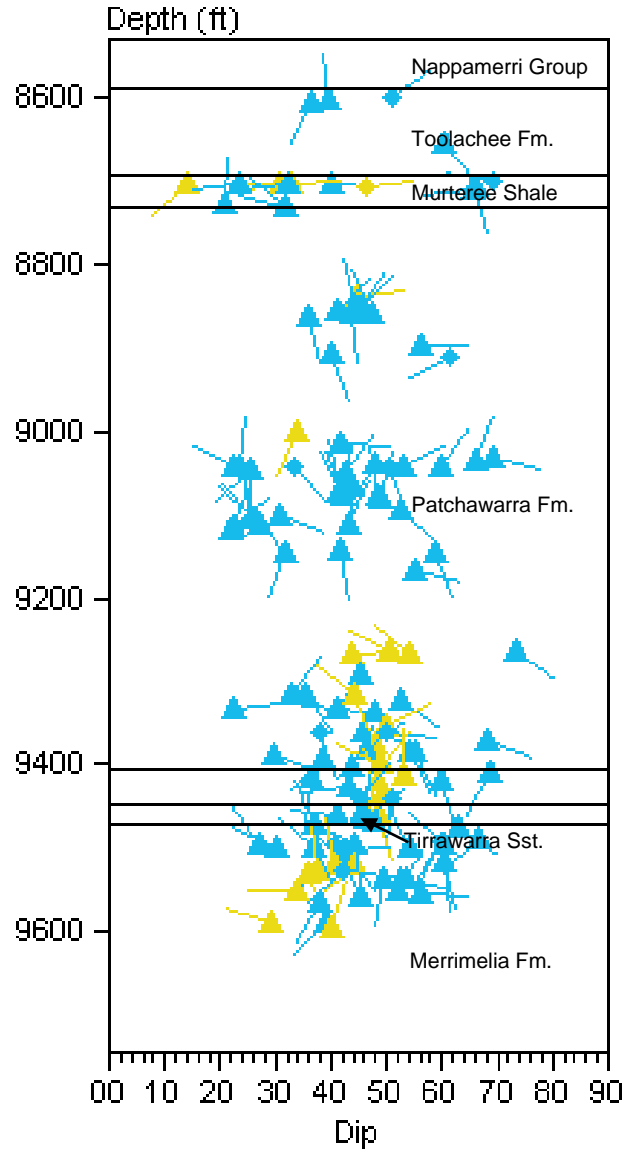


Figure 12 Summary of fracture orientation and distribution within Well A identified from STAR resistivity images. Rose plots superimposed on stereonet with faults plotted as poles to planes (southern hemisphere projection) where blue points are conductive faults and orange points are resistive faults.

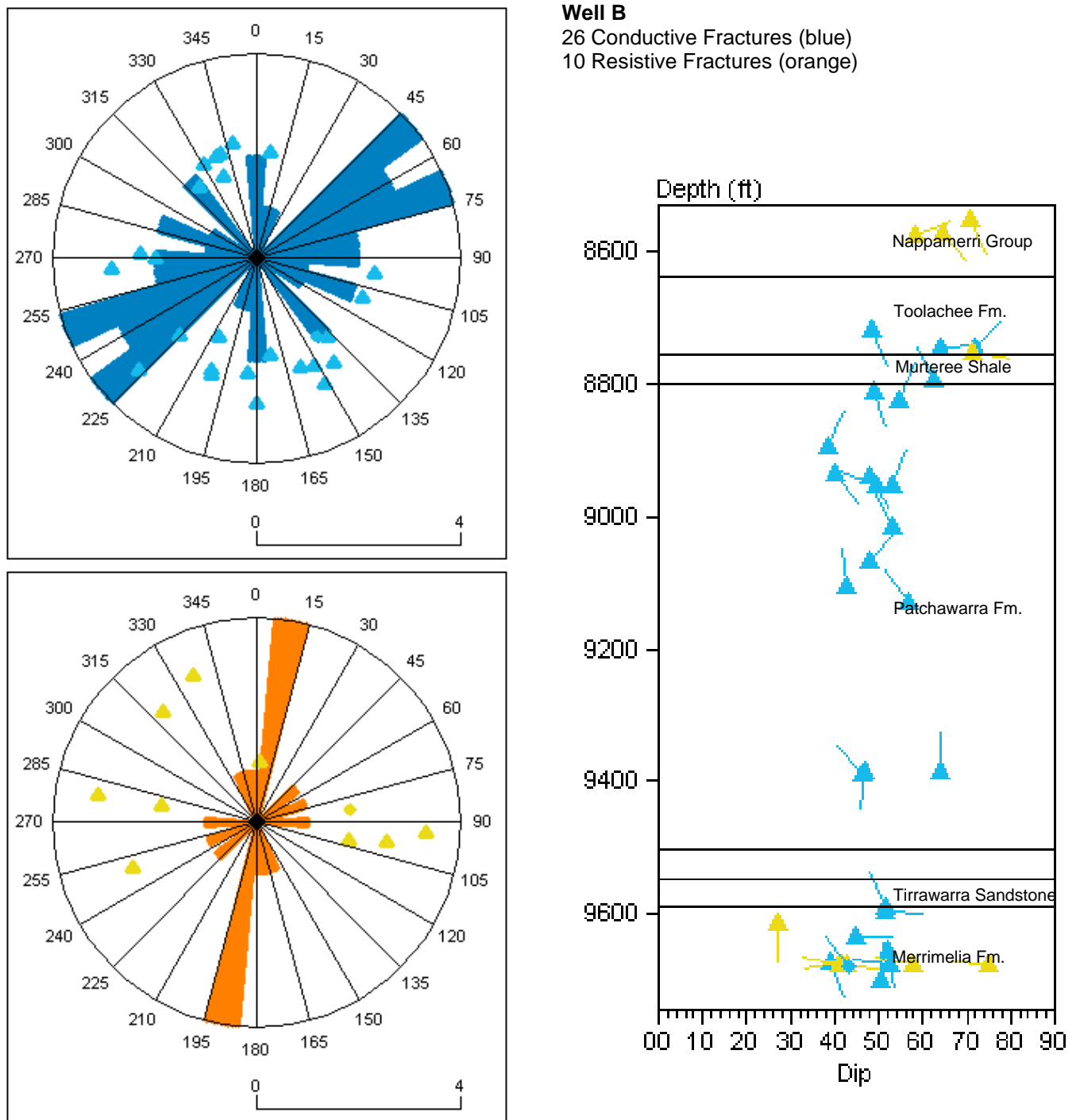
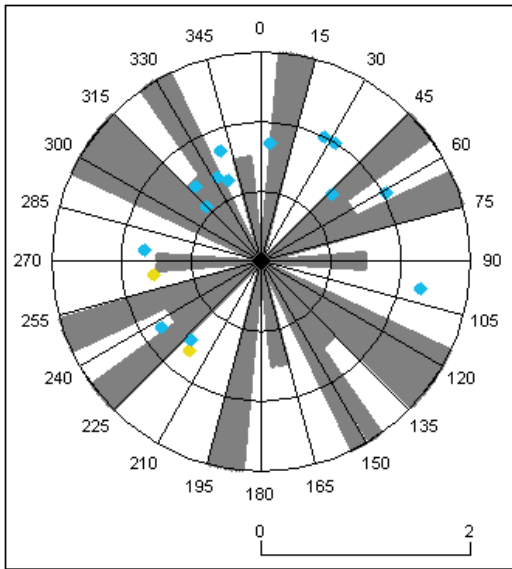


Figure 13 Summary of fracture orientation and distribution within Well B identified from STAR resistivity images. Rose plots superimposed on stereonet with faults plotted as poles to planes (southern hemisphere projection) where blue points are conductive faults and orange points are resistive faults.

Well A Faults



Well B Faults

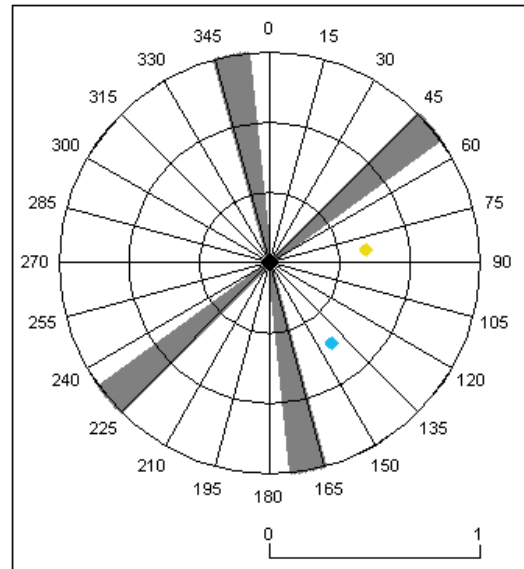


Figure 14 Summary of fault orientations within Well A and Well B where a fault is defines as a fracture with obvious displacement as identified from STAR resistivity images. Rose plots superimposed on stereonet with faults plotted as poles to planes (southern hemisphere projection) where blue points are conductive faults and orange points are resistive faults.

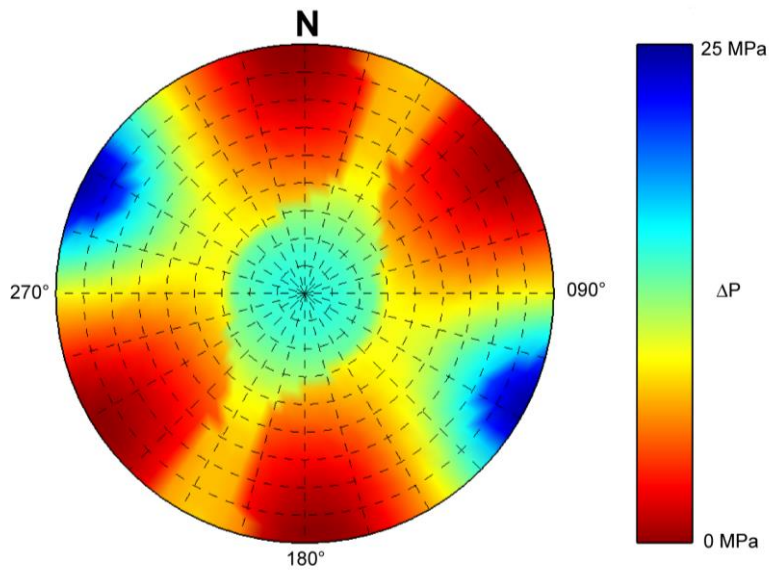


Figure 15 Fracture susceptibility model for Field A which contours all fracture orientations relative to their susceptibility of being hydraulically conductive within the contemporary stress environment. ΔP is the pressure required to initiate failure and is measured in MPa. All points are plotted as poles to planes on a southern hemisphere projection stereonet.

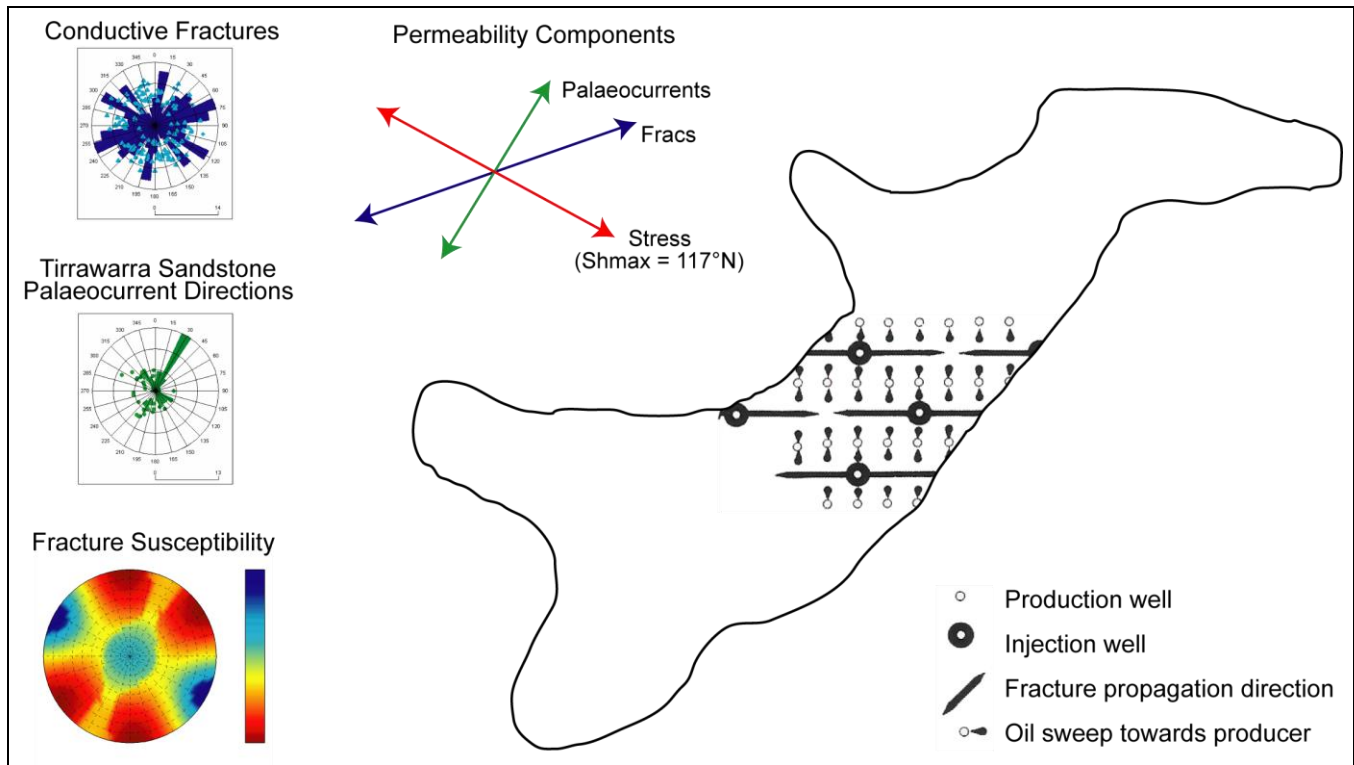


Figure 16 Schematic representation of permeability components identified at Field A and proposed injector-producer well array to maximise sweep efficiency. Well array schematic taken from Bell (1990).